Microstructure of Cs-implanted zirconia: Role of temperature

L. Vincent, L. Thome, F. Garrido, O. Kaitasov, Florent Houdellier

Microstructure of Cs-implanted zirconia: Role of temperature

L. Vincent, L. Thomé, F. Garrido, O. Kaitasov, and F. Houdelier

Citation: Journal of Applied Physics **104**, 114904 (2008); doi: 10.1063/1.3021162
View online: https://doi.org/10.1063/1.3021162
View Table of Contents: http://aip.scitation.org/toc/jap/104/11
Published by the American Institute of Physics

Microstructure of Cs-implanted zirconia: Role of temperature

L. Vincent,[1,a)] L. Thomé,[1] F. Garrido,[1] O. Kaitasov,[1] and F. Houdelier[2]
[1]*CSNSM-UMR8609, CNRS-IN2P3-Université Paris-Sud, F-91405 Orsay-Campus, France*
[2]*CEMES-UPR8011, CNRS 29, rue Marvig BP 94347, 31055 Toulouse Cedex 4, France*

(Received 1 July 2008; accepted 3 October 2008; published online 4 December 2008)

The aim of this study was to identify experimentally the phase which includes cesium in yttria stabilized zirconia (YSZ). The solubility and retention of cesium in YSZ were studied at high temperature (HT). Cesium was ion implanted (at 300 keV) into YSZ at room temperature (RT), 750 °C, or 900 °C at fluences up to 5×10^{16} cm^{-2}. The temperature dependence of the radiation-induced damage and of the cesium distribution in YSZ single crystals was investigated by Rutherford backscattering spectrometry and ion channeling. Transmission electron microscopy (TEM) studies were performed in order to determine the damage nature and search for a predicted ternary phase of cesium zirconate. Whatever the implantation temperature, the thickness of the damaged layer increases inwards with ion fluence. At RT, amorphization occurs, caused by the high Cs concentration (7 at. %). *In situ* TEM during postannealing shows recrystallization of cubic zirconia after release of cesium. A high implantation temperature has a significant influence on the nature of radiation defects and on the retained Cs concentration. At HT, dislocation loops and voids are formed but no amorphization is observed whereas polygonization occurs at high fluence. The implanted cesium concentration reaches a saturation value of 1.5 at. % above which Cs can no longer be retained in the matrix and is then released at the surface. At that concentration, cesium forms a solid solution in YSZ; no other phase is formed, neither during irradiation nor after thermal annealing. © *2008 American Institute of Physics*. [DOI: 10.1063/1.3021162]

I. INTRODUCTION

Over the past decade, the concept of actinide destruction in inert matrix fuels (IMFs) has received increasing attention worldwide.[1–3] This approach allows a significant reduction of the Pu and minor actinide contents when using uranium-free fuel. Based on neutron irradiation-related and thermodynamic properties, numerous refractory ceramics have been selected for use as IMFs.[4] Despite its low thermal conductivity, yttria-stabilized cubic zirconia (YSZ) is considered to be one of the most promising IMFs[5,6] since it is chemically stable and may form solid solutions with high concentrations of actinide dioxides.[7] Therefore, this advanced fuel is foreseen as to be used in light water reactors and then directly sent to a final geological depository. Its exceptional radiation damage resistance under neutron irradiation[8] and low-energy ion bombardment[9–11] has been demonstrated. YSZ does not undergo amorphization under heavy noble-gas implantation up to high displacement per atom (dpa) levels. Amorphization was only observed under Cs implantation at room temperature (RT).[12] This structural transformation is more likely due to the chemical effect of incorporated Cs than resulting from atom displacements and was suggested by Wang *et al.*[12] to be caused by the Cs^+ misfit in the YSZ structure due to its valence and its large ionic radius (165 pm) compared to the host atoms. The authors also emphasized the low mobility of Cs at RT.

Another crucial criterion to make use of YSZ as an IMF and waste form is its ability to confine radiotoxic fission products in both of the potential utilization conditions, i.e., medium temperature for disposal and high temperature (HT) during burn up. This issue has only received little attention,[13–18] especially regarding Cs retention at HT. The low thermal conductivity of YSZ implies that the IMF could reach very high operating temperatures (up to 1800 °C) in a reactor.[19,20] Under such conditions, Cs diffusion, release, and/or precipitation are expected. Thus it is essential to study the solubility of Cs in YSZ at HT. In addition, the formation of cesium zirconate (Cs_2ZrO_3) was predicted by several authors.[21,22] Thermodynamic calculations performed by Pouchon *et al.*[14] predicted the stability of this ternary phase up to 900 °C, and the solubility limit of Cs (up to 1700 °C) was estimated to be 1.5 at. %. From this relatively low solubility value, one can expect that Cs atoms may escape from the matrix or precipitate as cesium zirconate at HT.

The purpose of the present work was to determine experimentally the phase in which Cs resides in YSZ at HT, i.e., as a solid solution or in cesium zirconate precipitates. For this purpose, ion implantation was used to incorporate Cs atoms in a YSZ matrix with related low-energy radiation damage (simulating damage created during reactor operation). In order to observe the possible formation of fission product precipitates and to determine the nature of the damage created by implantation, we combined transmission electron microscopy (TEM) experiments and *in situ* Rutherford backscattering spectrometry in channeling mode (RBS/C) on YSZ single crystals implanted with Cs ions at various temperatures. The results presented here are organized in four sections. First, we summarize results on damage buildup in Cs-implanted YSZ at different temperatures. In the second

[a)]Author to whom correspondence should be addressed. Electronic mail: laetitia.vincent@csnsm.in2p3.fr. Tel.: +33169155231. FAX: +33169155268.

TABLE I. Implantation parameters and values of dpa and concentration calculated by TRIM for selected fluences of Cs.

Energy (keV)	Fluence (cm^{-2})	dpa	C_{max} (at. %)
70	3×10^{14}	0.9	0.2
300	3×10^{14}	1.3	0.05
300	9×10^{14}	3.8	0.16
300	5×10^{15}	21	0.92
300	10^{16}	43	1.84
300	5×10^{16}	213	9.2

and third sections, we discuss TEM results that provide information on the nature and distribution of defects created at RT or at HT, viz., 750 and 900 °C. Then we consider the retention of Cs in the matrix. Finally we discuss all our results and conclude concerning the evolution of the damage and the solubility of Cs in YSZ.

II. EXPERIMENTAL

The specimens used in the present study are YSZ single crystals (⟨100⟩ orientation) containing 9.5 mol % Y_2O_3, synthesized by Crystal-GmbH. All samples were coated with a conductive carbon layer (thickness adapted to the characterization technique) in order to avoid charging under ion or electron beam irradiation.

Bulk samples were implanted with increasing fluences of Cs ions at RT, 750 °C, and 900 °C. The ion flux was $\sim3\times10^{11}$ cm^{-2} s^{-1}. An incident beam angle of 7° was used to avoid channeling. The Cs^{2+} ion energy was 300 keV, leading to a projected range of about $R_p=67$ nm and range straggling approximately $\Delta R_p=25$ nm. The depth distribution of the implanted species and the number of dpa were estimated via the TRIM code[23] assuming a displacement energy of 40 eV. Table I indicates (for each fluence) the dpa equivalent at the defects distribution maximum and the maximum Cs concentration estimated from TRIM.

RBS/C analyses were carried out *in situ* with the IRMA/ARAMIS facility of CSNSM-Orsay.[24] A two-axis goniometer was specifically developed to allow HT implantation and RBS/C measurements. The temperature was measured by a thermocouple fixed on the sample holder. During implantation, the temperature stability was better than 5 °C. Fluences were incremented from 10^{14} up to 5×10^{16} cm^{-2}. After each implantation step, RBS/C measurements were performed near RT with a 3.065 MeV He^{2+} beam at a detection angle of 165°. The energy resolution of the electronic setup was 15 keV corresponding to a depth resolution better than 10 nm at the YSZ surface.

Several implanted samples were cut and thinned for plan view and cross-section TEM (XTEM) at 200 and 300 kV. The thermal evolution of damage in RT preimplanted XTEM samples was studied *in situ* after successive isochronal (15 min) anneals using a double tilt TEM hot stage from 300 to 750 °C, and a final anneal was performed for 1 h at 750 °C. High resolution TEM (HRTEM) was carried out using the SACTEM-Toulouse, a Tecnai F20 ST (FEI) fitted with an imaging aberration corrector (CEOS), a 2000 charge-coupled device camera (Gatan), and imaging filter (Gatan Tridiem).

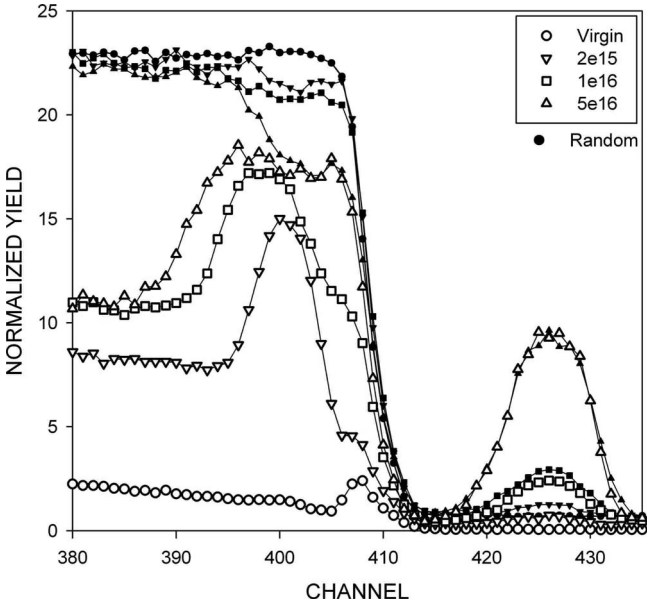

FIG. 1. High-energy part of RBS spectra recorded in random (filled symbols) and ⟨100⟩-axial (open symbols) directions on YSZ crystals implanted with 300 keV Cs ions at RT. The Cs peaks are located around the channel 425. A background due to the presence of Hf impurities in YSZ is superimposed to the Cs signal and is deconvoluted during analysis. Damage accumulation is noticeable on the axial spectra in the channel range [390–410]. Depth profiles and kinetics of disorder yield are extracted from the analysis of these spectra.

In addition, the structural evolution as a function of the fluence was investigated *in situ* with a Philips CM12 transmission electron microscope on line with the IRMA ion implanter.[25] TEM samples were implanted at RT and 750 °C with 70 keV Cs^+ ions ($R_p=20$ nm and $\Delta R_p=8$ nm). Cs fluences varied from 10^{14} up to 5×10^{15} cm^{-2}. TRIM calculations indicate that for the same Cs fluence, the number of dpa at the maximum of the defect distribution is about 30% lower at 70 keV than at the energy used for RBS/C in bulk samples (300 keV) (see Table I).

III. RESULTS

RBS/C was used for quantitative measurement of the lattice disorder and of the implanted Cs concentration. TEM observations provide qualitative complementary information on the damaged structure at the main steps of the damage kinetics. This approach was used to determine the influence of temperature on the nature of created defects and on Cs diffusion and/or precipitation. In the first subsection, we compare the damage buildup at different temperatures. Then we present results obtained on the structure of Cs-implanted YSZ at RT. Results are also given on the effect of a thermal post-anneal. In the third section, we focus on the nature of defects created by HT implantation. Finally, Cs depth profiles are examined to determine Cs solubility in YSZ at HT.

A. Disorder buildup

From RBS/C spectra, one can obtain the impurity concentration and the fractional lattice disorder (f_D). The methodology was described elsewhere.[26] Figure 1 shows the high-

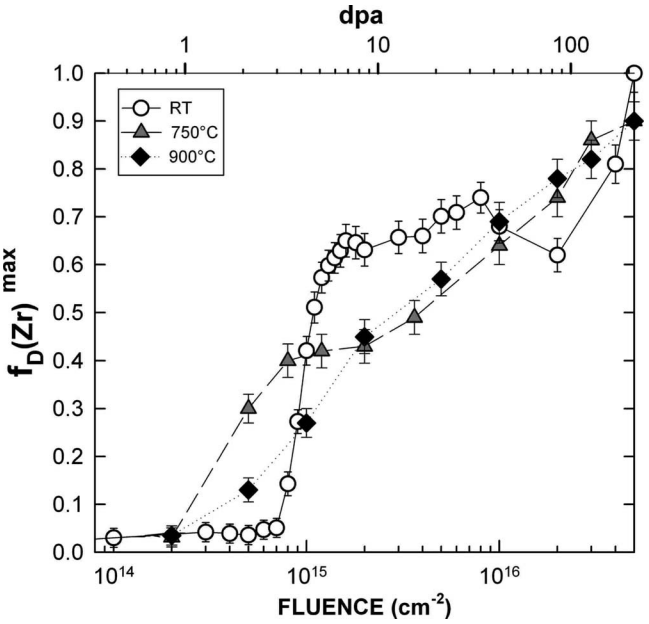

FIG. 2. Damage accumulated as a function of the fluence (and vs dpa on the top scale) in YSZ crystals implanted with 300 keV Cs ions at RT (open circles), 750 °C (triangles) and 900 °C (rhombs). The value of $f_{D\max}$ is taken at the maximum of the damage peak in Fig. 1.

energy part of typical RBS/C spectra recorded along the ⟨100⟩ axis on YSZ crystals implanted with increasing Cs ion fluences at RT. The analysis of the Cs peak around channel 425 provides the Cs depth distribution, as discussed in the last section below. In the YSZ near-surface section of the "random" spectra, the backscattering yield is reduced as the fluence increases due to the relative concentration increase in Cs in the matrix. The analysis of the damage peak between channel 390 and 410 gives the depth profiles of f_D created in the Zr sublattice of the crystal. This disorder increases with increasing fluence. Hence, we can follow the damage buildup which is the amount of damage ($f_{D\max}$) accumulated at the maximum of the damage peak as a function of the fluence (or the dpa).

Figure 2 shows the plots of the damage buildup, for the three implantation temperatures RT, 750 °C, and 900 °C. At RT, the damage buildup clearly exhibits distinct stages: (1) a plateau characterized by a very low damage level, (2) a transitional rise of the disorder level around 10^{15} ions cm^{-2} (4 dpa), (3) a slowly rising plateau, (4) a small decrease between 8×10^{15} and 2×10^{16} cm^{-2}, and (5) a sharp increase up to $f_{D\max}=1$. By contrast, at HT, the disorder stages are poorly defined. The damage kinetics increase practically linearly with the fluence (except for a small plateau observed at 750 °C between 8×10^{14} and 2×10^{15} cm^{-2}). In the range from 10^{14} to 8×10^{14} cm^{-2}, very little disorder is produced at RT, whereas the damage yield increases noticeably at 750 and 900 °C. However, for fluences between 10^{15} and 10^{16} cm^{-2}, $f_{D\max}$ is much lower at HT than at RT. Moreover, $f_{D\max}$ reaches a value of 1 at RT, a feature which is consistent with TEM observations showing amorphization at 5×10^{16} cm^{-2} (see below), whereas disorder is not complete at HT for the same fluence.

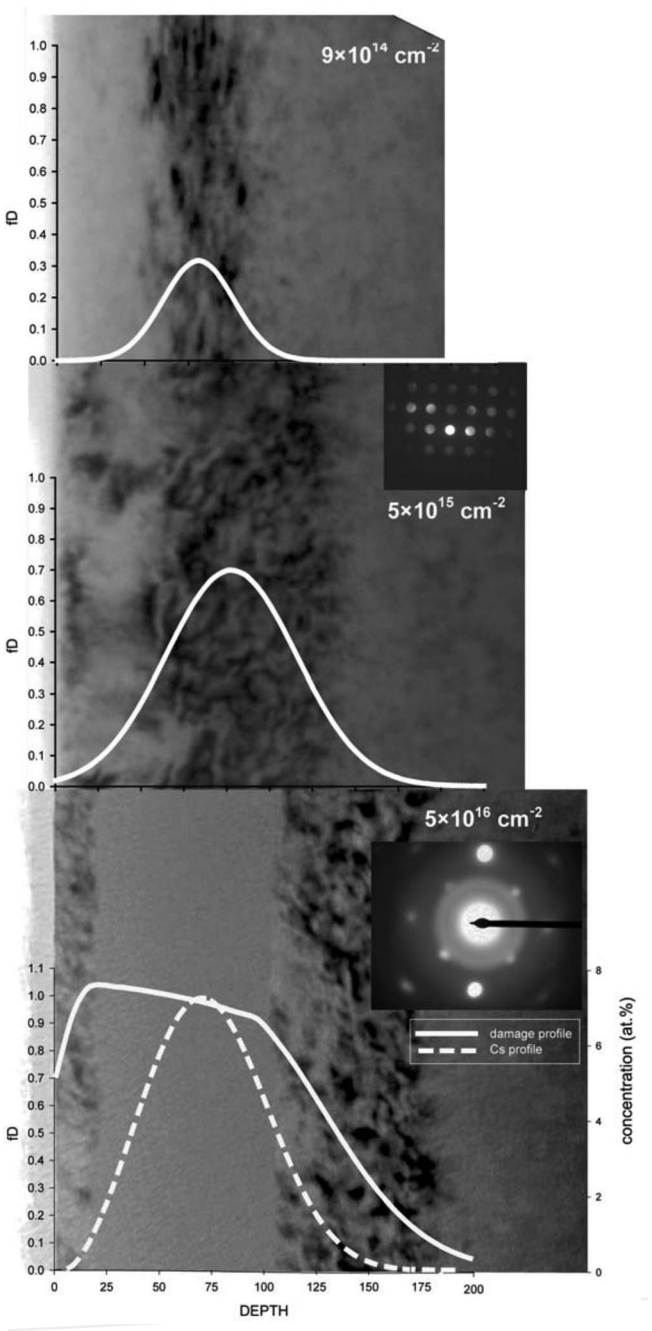

FIG. 3. Bright-field TEM micrographs of YSZ implanted with 300 keV Cs ions at RT for increasing fluences. Diffraction patterns shown in inset were taken on damaged zone. At the same spatial scale, disorder (f_D) profiles measured by RBS/C are given for comparison. At 5×10^{16} cm^{-2}, is also given the measured Cs distribution measured by RBS.

B. Microstructure after RT implantation and thermal annealing

1. Structure of as-implanted YSZ at RT

We studied via TEM the YSZ damaged layer structure as a function of the 300 keV Cs ion fluence up to 5×10^{16} cm^{-2}. Bright-field TEM micrographs recorded on cross sections of RT-implanted samples are shown in Fig. 3 and compared to damage and Cs profiles obtained via RBS/C. At low fluence, below 5×10^{15} cm^{-2}, the implanted layer shows three distinct regions; an almost defect-free surface layer of 40 nm above a heavily damaged zone followed

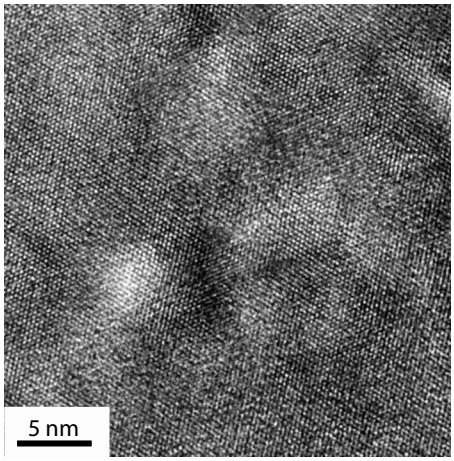

FIG. 4. HRTEM micrograph showing the distorted areas in YSZ after Cs implantation at RT with a fluence of 9×10^{14} cm^{-2}.

by the virgin substrate. Initially the damaged zone was centered at a depth $d=64\pm2$ nm, close to $R_p=67$ nm calculated from the TRIM code. As the ion fluence increases, the damaged layer expands toward greater depths, while the surface layer is slightly damaged. The depth and width measurements of the damaged layer are in good agreement with defect profiles obtained from RBS/C. Up to 5×10^{15} cm^{-2} (i.e., 21 dpa), diffraction patterns of the damaged zone (inset of Fig. 3) shows a residual crystalline structure and the absence of extra reflections. No secondary or amorphous phase is evidenced. Diffraction contrasts are not consistent with the presence of dislocation loops. They are rather diffuse dots which do not display a specific Burgers vector. In Xe-implanted samples, we previously observed identical defect clusters in the same dpa range.[27] Thus, these clusters are not produced by a chemical effect due to Cs. HRTEM observations carried out on the sample implanted with 9×10^{14} cm^{-2} Cs ions reveal a mosaic of nanometer-sized domains with a distorted lattice. These distorted areas induce large strain fields, causing spatial variations of the contrast in their vicinity (Fig. 4). This micrograph also confirms the absence of any amorphous region, which would present an aperiodic structure.

At high fluence (5×10^{16} cm^{-2}), Cs implantation leads to the formation of an amorphous layer whereas YSZ did not undergo amorphization under Xe irradiation up to high fluences.[11,28] The amorphous character is observable on the micrograph (Fig. 3) via the loss of diffraction contrast in the central part. This layer (between 20 and 105 nm) agrees very well with the RBS/C damage profile and corresponds to $f_D\sim1$. The amorphous character is also confirmed by the presence of a diffuse ring in the selected area electron diffraction (SAED) pattern. No secondary phase is observed. Complementary *in situ* experiments (at 70 keV) established via the occurrence of a ring on the SAED pattern that amorphization occurs at a fluence threshold of 4×10^{16} cm^{-2}, corresponding to a concentration of about 2.3 at. % at R_p, according to the TRIM code.

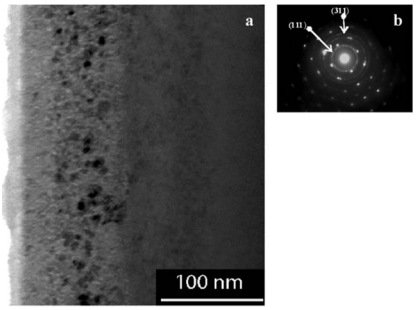

FIG. 5. (a) Bright-field underfocus TEM micrograph of YSZ implanted with 300 keV Cs ions (5×10^{16} cm^{-2}) and annealed at 750 °C during 1 h. Recrystallization occurs by the formation of rounded nanocrystals. Between crystallites, cavities are visible in this underfocused image. Note that in off-Bragg conditions, the contrasts of distorted domains created in the deeper crystalline damaged zone are not visible here but they are present as these defects are not annealed at this temperature. (b) Diffraction pattern corresponding to the TEM image. Non epitaxial recrystallization is associated with the apparition of rings corresponding to the YSZ lattice parameters.

2. Microstructure after RT implantation and annealing

Thermal treatment of implanted bulk samples was performed up to 750 °C in order to follow the thermodynamic evolution of defects and to study the possibility of secondary phase formation. Annealing was carried out *in situ* on cross-sectional TEM samples. No structural modification was detected on samples implanted with 5×10^{15} cm^{-2}. Thus, the defects formed at this implantation fluence are thermally stable up to 750 °C. Conversely, the amorphous zone observed at 5×10^{16} cm^{-2} undergoes nonepitaxial recrystallization, as shown in Fig. 5. This recrystallization starts at 600 °C. The micrograph recorded in off-Bragg conditions shows rounded crystallites in the previously amorphized zone. On the SAED pattern, we easily identified the diffraction rings consistent with the (200) and (220) spots. Additional rings were indexed and correspond to the distance d_{hkl} of the cubic zirconia. The (111) and (311) rings are marked (arrows) in Fig. 5(b). We observed no other phase. Previous experiments[29] showed almost total release of implanted Cs above a temperature threshold of 600 °C. Thus, we conclude that the recrystallization of Cs-rich amorphous YSZ occurs concurrently with the release of Cs atoms. It is worth noting that cavities are formed in the recrystallized area as well as in the surface layer.

3. Microstructure after HT implantation

Cs implantations were also performed at 750 and 900 °C in bulk samples. To follow the damage buildup at low fluence, TEM experiments were performed *in situ* during Cs implantation at 70 keV. Figure 6 compares, at RT and 750 °C, the microstructures of the samples implanted at 3×10^{14} cm^{-2} (i.e., 0.9 dpa). The structure and size of defects are obviously affected by the implantation temperature. At RT [Fig. 6(a)], small diffuse dots are observed (with a diameter below 7 nm). This mottled feature consists of distorted nanodomains as demonstrated previously. At 750 °C, the implanted sample is clearly more damaged and point defects have coalesced to form dislocation loops with a size ranging from 10 to 20 nm [Fig. 6(b)]. The dislocation loop density

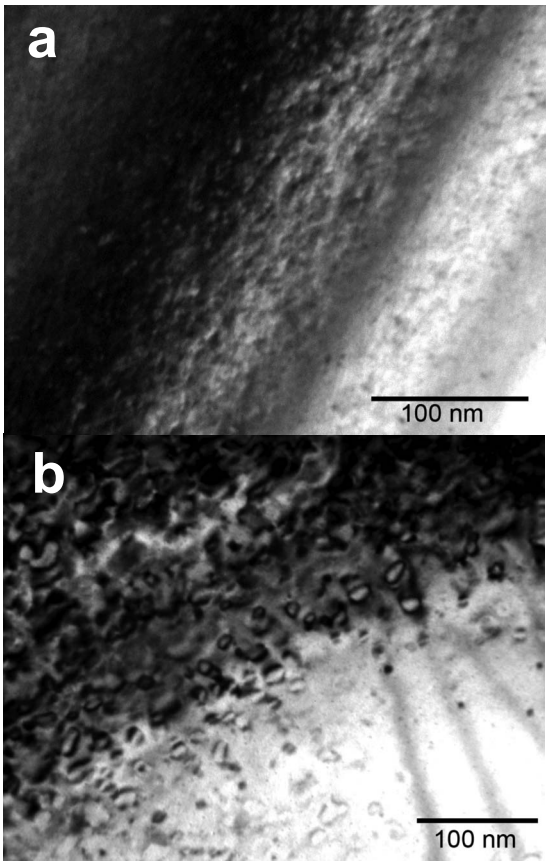

FIG. 6. Bright-field TEM micrographs of YSZ implanted *in situ* with 70 keV Cs ions (3×10^{14} cm^{-2}, 0.9 dpa) (a) at RT and (b) at 750 °C. Images were recorded in Bragg conditions using $g=111$.

increases with fluence. These observations agree with the continuous buildup of f_D at HT observed by RBS/C. The nature of these loops is currently under investigation. Preliminary results indicate that they are probably perfect interstitial-type dislocation loops.

At higher fluence, the structural evolution was observed by TEM on cross-sectional samples implanted with 300 keV Cs ions. The damage zone undergoes significant broadening with increasing fluence. Above 10^{16} cm^{-2} (1.8 at. %), the damaged layer exhibits two different microstructures as a function of depth (Fig. 7). (1) The subsurface (which expands up to 60 nm) contains bubbles, and (2) the deeper zone (between 60 and 150 nm) shows dislocation loops. When the defects were tilted away from contrast, we observed cracks in the damaged region. These fractures are mostly situated at the end of the bubble zone. The results are similar for both temperatures, the bubble and fracture sizes being larger at 900 °C. Increasing the fluence up to 5×10^{16} cm^{-2} induces bubble growth at the surface and their expansion toward greater depth (115 nm), but does not lead to amorphization (Fig. 8). The SAED pattern shown in the inset of Fig. 8 confirms the absence of amorphization and exhibits satellite spots near some of the main Bragg reflections. These extra spots are related to Moiré fringes sometimes visible on micrographs recorded under two-beam conditions. They are presumably due to grain misorientation. The diffraction pattern reveals no precipitation of any additional phase. Assuming rotation, the distance between the main spot and the extra one was measured on a series of diffraction patterns and corresponds to a mean angle of 5°. HRTEM observations were carried out to confirm the formation of low-angle grain boundaries. Figure 9 clearly shows two domains having lattice planes misoriented by about 8°. The position of some dislocations is indicated (arrows) on the figure. They are aligned to form a boundary between the two domains. The Fourier transform of this micrograph indicates the presence of two sets of zone axis patterns rotated relative to each other. Therefore, a temperature increase during implantation leads neither to formation of cesium zirconate nor other solid precipitates in the matrix, nor to amorphization, but enhances dislocation mobility, resulting in polygonization.

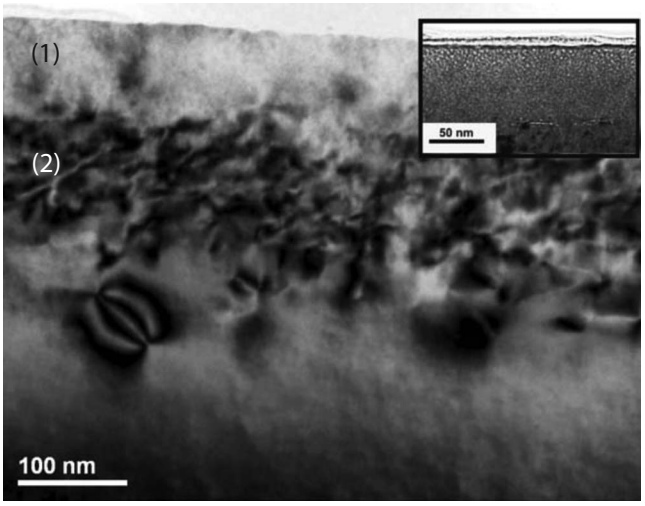

FIG. 7. Bright-field TEM micrographs of YSZ implanted with 300 keV Cs ions (1×10^{16} cm^{-2}) at 900 °C. The general view shows the overall damaged zone with two beam dynamical conditions. In inset is presented, with the same space scale, the subsurface layer recorded with off-Bragg and underfocus image conditions showing the presence of bubbles.

4. Cs solubility

Depth distributions of implanted Cs atoms were deduced from random RBS spectra and compared at RT and 900 °C (Fig. 10). Concentrations expected at the maximum of Cs

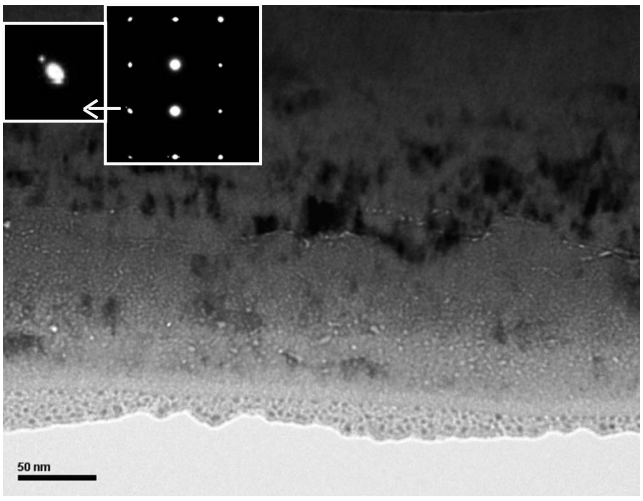

FIG. 8. Under focus TEM micrograph recorded in off-Bragg condition on a cross section of YSZ implanted with 5×10^{16} cm^{-2} Cs ions at 900 °C.

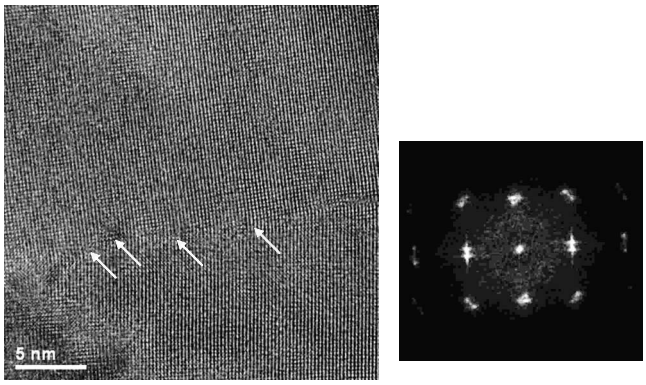

FIG. 9. On the right, an HRTEM image showing the polygonization of YSZ implanted at 900 °C (5×10^{16} cm^{-2}). Arrows indicate the localization of some dislocation on the boundary. On the left, the Fourier transform of the micrograph shows two sets of zone axis pattern corresponding to the observed two domains rotated relatively to each other.

profile (C_{max}), simulated by TRIM, are shown in Table I. At low fluence, the experimental concentrations were in excellent agreement with the TRIM values and the profiles were similar at both implantation temperatures. At high fluences, Cs distributions plotted in Fig. 10 depended strongly on the implantation temperature. At RT, the concentration increased with fluence. At 5×10^{16} cm^{-2}, C_{max} as measured by RBS was about 18% below the value expected from TRIM (9.2 at. %). This is likely due to sputtering during implantation, not accounted for in our TRIM calculations. At 1×10^{16} cm^{-2}, the measured C_{max} at HT was slightly lower than at RT. Moreover, for higher fluences (3×10^{16} cm^{-2}), the concentration at HT did not increase as expected from TRIM calculations, but saturated at about 1.5 at. %. The Cs distribution at HT also showed Cs diffusion and significant release at the surface. Finally, at 5×10^{16} cm^{-2} C_{max} was about 1.4 at. % when Cs was implanted at HT, whereas 7 at. % of Cs was retained in the matrix at RT.

Previously we pointed out bubble formation in the subsurface of YSZ (up to 60 nm) at 900 °C and at a fluence of 1×10^{16} cm^{-2}. A comparison of Figs. 7 and 10 shows that those bubbles are not located at the Cs peak maximum, but

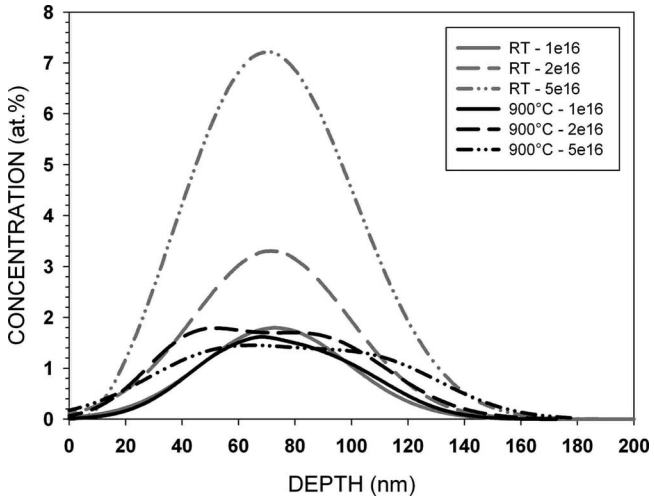

FIG. 10. Cs profiles obtained by RBS in random direction on YSZ implanted at RT and 900 °C with increasing fluences.

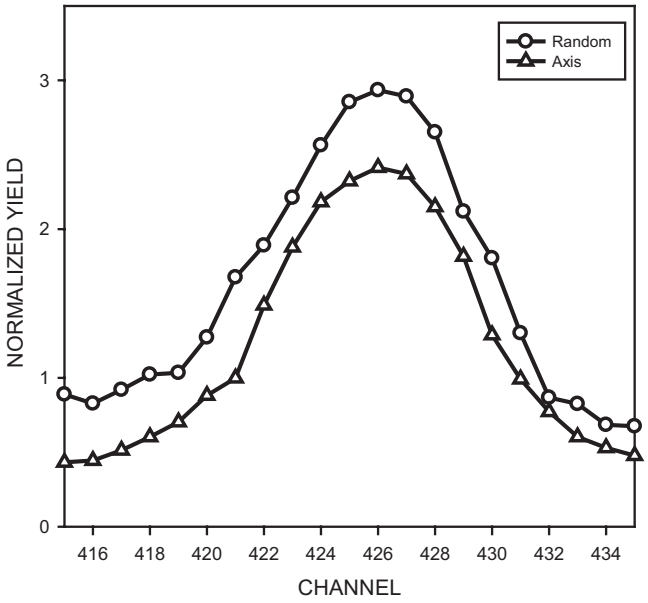

FIG. 11. RBS spectra recorded in random and axial direction in the channel range [415–435] corresponding to the Cs signal in YSZ implanted at RT with 1×10^{16} cm^{-2}.

are formed between the surface and C_{max}. The high bubble density in the first 20 nm below the surface, where the Cs concentration vanishes, supports the idea that most of the bubbles are in fact voids. Note that they are observable above a fluence of 1×10^{16} cm^{-2} when the Cs concentration tends to saturate. The formation of large voids is thus likely related to Cs release.

Spectra recorded in the channel range [415–435] show a rather large difference depending on whether the analyzing beam is oriented in the random or axial direction, as shown in Fig. 11. In this region of interest, the normalized yield is related to the backscattering on Cs atoms. The peak acquired along the major ⟨100⟩ axis exhibits significant lower values than in the random direction. This feature can be explained by assuming that a fraction of Cs atoms is located in substitutional lattice sites of the cubic matrix. Accordingly, a solid solution is rather formed instead of cesium zirconate precipitates. This observation is in agreement with the absence of incoherent precipitates checked on SAED patterns. In addition, no evidence of coherent precipitates, such as Ashby–Brown contrasts[30] was found in TEM micrographs, and electron energy loss spectrometry measurements displayed a low and homogeneous repartition of Cs in the TEM cross-sectional sample along the damaged zone. Thus, we conclude that Cs atoms form a solid solution in YSZ at HT with a solubility limit of 1.5 at. %.

IV. DISCUSSION

The results give insight as to the influence of the implantation temperature on the structural evolution of cubic zirconia and on Cs retention in this material. RBS/C data showed that disorder accumulation is largely dependent on the implantation temperature (Fig. 2).

For RT implantation, the buildup shows the usual shape of a transitional rise between two plateaus, followed by a

second rapid increase up to amorphization. This latter step only occurs in the case of Cs implantation (not for noble gas atoms). This variation of $f_{D\max}$ exhibits a typical multistep damage accumulation (MSDA) process which may thus be accounted for with the MSDA model.[31] Both transitions are related to a collapse of the crystalline structure. The driving force of this transformation is obviously the free energy reduction of the damaged crystal. The first stage observed at low fluences (below 3 dpa) corresponds to the formation of point defects and of tiny distorted nanodomains producing stress fields within the matrix. The stress, inducing a high increase in elastic energy, is likely relaxed by the local formation of dislocations. The sharp increase in $f_{D\max}$ (ranging from 3 to 5 dpa) is due to the overlapping of these coherent domains (Fig. 3), which may generate misfit dislocations in order to decrease the stored elastic energy. The plateau observed above 6–7 dpa likely corresponds to a saturation of the number of domains and dislocations, accompanied by a broadening of the damage layer. These first three stages are commonly observed with heavy ion implantation. They are assumed to come from ballistic effects. Up until now, no clear explanation could be proposed for the decrease of $f_{D\max}$ between 1×10^{16} and 2×10^{16} (cf. Figure 2). Finally the second rise at high fluence is due to a chemical effect induced by the high Cs concentration. The Cs ions can no longer be incorporated in the crystalline structure, and the system minimizes its chemical potential by a phase transformation to the amorphous state. Therefore, two successive ballistic and chemical processes are responsible for the damage buildup in cubic zirconia implanted at RT with Cs ions. They are respectively defined by the number of dpa and the impurity concentration.

At HT, the monotonous increase of $f_{D\max}$ versus the fluence can no longer be represented by a MSDA process or by single-step models such as the direct impact and cascade overlap proposed by Gibbons[32] or the direct impact/defect stimulated model.[33] These models show, respectively, exponential rise or sigmoidal-shaped dependencies of the disorder versus fluence. The rapid increase of the disorder measured by RBS/C at low fluences (starting at 1 dpa) is due to the early formation of large extended defects. The HT promotes the diffusion and precipitation of point defects to form dislocation loops. The loop density rises with fluence in accordance with the linear increase of $f_{D\max}$. At high fluence, overlap of the associated stress field of dislocations may be reached. At 5×10^{16} cm^{-2}, the stored energy might be too high, and mobile dislocations condense to form low-angle grain boundaries and subgrains. This phenomenon does not seem to be transitional in type but rather corresponds to a continuous thermally activated dynamic recovery. The increase in $f_{D\max}$ at the highest fluences is due to the rotation of subgrains which causes a large direct backscattering of the analyzing beam. Polygonization is a well-known process which allows the system to reduce its elastic energy by rearrangement and annihilation of dislocations. The thermal contribution during implantation allows continuous minimization of the stored energy in the defective structure, while at RT the damage evolves by discrete structural transformations when the corresponding energetic barrier has been overcome. It is worth noting that the static recovery after thermal annealing of the amorphized layer at RT does not lead to polygonization with low-angle grain boundaries but rather results in a recovered polycrystalline YSZ. The driving force for recrystallization could be the release of Cs atoms above 600 °C. Further experiments using x-ray diffraction measurements are in progress to follow stress evolution as a function of fluence. According to the present results, we believe that at RT stress should increase drastically in the fluence range corresponding to the plateaus of damage buildup and the transitional rises should be associated to stress relaxation due to structural collapse. On the contrary at HT, stress increase as a function of fluence is expected to be monotonous.

Whereas cesium zirconate precipitation was predicted to occur at HT,[14,21,22] no extra reflections were found in our SAED patterns to confirm the existence of an incoherent phase up to the final fluence of 5×10^{16} cm^{-2}, neither after post-thermal treatment, nor after HT implantation. Previous experiments[29] showed that thermal postannealing induces significant Cs release above 600 °C. The remaining concentration falls to 1.5 at. %, i.e., close to the solubility limit estimated by Pouchon *et al.*[14] We assume that the recrystallization of amorphous Cs-rich YSZ is due to the concentration decrease of Cs atoms. Thermal contribution during implantation also enhances the release at the surface of Cs atoms, associated with the formation of voids. The concentration reaches a saturation value of 1.5 at. %. This result again confirms the calculated solubility limit of Pouchon *et al.*[14] At HT, Cs becomes volatile and acts as a gas in the matrix. However, the observed "bubbles" do not result from gas atom accumulation since they are actually cavities. The nucleation and growth of voids are due to clustering of mobile vacancies. However, it is now considered that gas atoms play a significant role in void nucleation, i.e., they are necessary to stabilize small vacancy clusters. Our results suggest that Cs atoms are not strongly trapped but are rather thermally dissociated from vacancy complexes and can migrate out of the matrix. Void growth likely takes place by vacancy absorption. The complete mechanism is not clearly identified. Further experiments are needed.

As regards the use of YSZ as IMF, the Cs concentration produced in the fuel must be lower than the solubility limit. On the other hand, the formation of voids and grain boundaries may be deleterious for the mechanical behavior of the matrix. Polygonization may be a general phenomenon at HT due to dislocation mobility. The chemical contribution does not seem to play a significant role in this process. Similar experiments should be performed with Xe ions to verify this point.

V. CONCLUSION

We have studied the temperature dependence of Cs retention in YSZ as well as the influence of temperature on the damage created by implantation. Results indicate that no precipitate crystalline phase is formed in YSZ whatever the implantation temperature. At RT, Cs concentration exceeds the solubility limit (1.5 at. %) and induces amorphization of the

matrix at a threshold of 2.5 at. %. On the contrary, Cs atoms cannot be retained in YSZ at concentration higher than 1.5 at. % above 750 °C. This temperature is foreseen to be exceeded in reactor operation. Contrary to what was expected from thermodynamical calculations, no precipitation of cesium zirconate is formed during HT implantation and Cs atoms remain in solid solution up to the solubility limit. As the temperature increases, Cs mobility is enhanced and Cs release toward the surface is observed without precipitation. The release mechanism is accompanied by void formation.

Damage buildup at RT evolves by discrete structural transformations. Two transitions are observed and are related to the reduction of free energy by collapse of the crystalline defective structure. Two successive mechanisms are involved in this damage evolution. First, a ballistic effect produces strained distorted nanodomains which relax by the formation of dislocations. Second a chemical contribution leads to amorphization. The amorphous layer is recrystallized by thermal annealing. Cs release is likely the necessary condition for this recrystallization. On the contrary, at HT, the disorder increases almost linearly with the ion fluence. Dislocation loops are formed and undergo rearrangement to form grain boundaries at high fluence. This polygonization induces grain rotation. We assume that this process takes place to continuously minimize the stored energy by precipitation of point defects in the defective structure, explaining why the buildup is no longer transitional. Heating during implantation allows dynamical recovery starting from the local rearrangement of dislocations whereas a postimplantation thermal anneal induces nonepitaxial recrystallization by nucleation of YSZ crystallites when Cs is released.

ACKNOWLEDGMENTS

The authors are grateful to the SEMIRAMIS team who made these experiments possible. We acknowledge M. Drouet for complementary high fluence implantations. We are indebted to the LSI in Palaiseau for open access to the microscope, especially to G. Rizza and G. Jaskierowicz. One of the authors would like to thank A. Claverie for helpful discussions on TEM results.

[1]C. Degueldre, U. Kasermeyer, F. Botta, and G. Ledergerber, Mater. Res. Soc. Symp. Proc. **412**, 15 (1996).
[2]C. Degueldre and J. M. Paratte, J. Nucl. Mater. **274**, 1 (1999).
[3]C. Degueldre, J. Alloys Compd. **444–445**, 36 (2007).
[4]H. Kleykamp, J. Nucl. Mater. **275**, 1 (1999).
[5]V. M. Oversby, C. C. McPheeters, C. Degueldre, and J. M. Paratte, J. Nucl. Mater. **245**, 17 (1997).
[6]G. Ledergerber, C. Degueldre, P. Heimgartner, M. A. Pouchon, and U. Kasemeyer, Prog. Nucl. Energy **38**, 301 (2001).
[7]W. L. Gong, W. Lutze, and R. C. Ewing, J. Nucl. Mater. **277**, 239 (2000).
[8]B. Savoini, D. Caceres, I. Vergara, R. Gonzalez, and J. E. Munoz Santiuste, J. Nucl. Mater. **277**, 199 (2000).
[9]W. J. Weber, R. C. Ewing, C. R. A. Catlow, T. Diaz de la Rubia, L. W. Hobbs, C. Kinoshita, H. Matzke, A. T. Motta, M. Nastasi, E. K. H. Salje, E. R. Vance, and S. J. Zinkle, J. Mater. Res. **13**, 1434 (1998).
[10]L. Thomé, J. Fradin, J. Jagielski, A. Gentils, S. E. Enescu, and F. Garrido, Eur. Phys. J.: Appl. Phys. **24**, 37 (2003).
[11]K. E. Sickafus, H. Matzke, T. Hartmann, K. Yasuda, J. A. Valdez, P. Chodak Iii, M. Nastasi, and R. A. Verrall, J. Nucl. Mater. **274**, 66 (1999).
[12]M. Wang, S. X. Wang, and R. C. Ewing, Philos. Mag. Lett. **80**, 341 (2000).
[13]M. A. Pouchon, M. Döbeli, and C. Degueldre, Nucl. Instrum. Methods Phys. Res. B **148**, 783 (1999).
[14]M. A. Pouchon, M. Dobeli, C. Degueldre, and M. Burghartz, J. Nucl. Mater. **274**, 61 (1999).
[15]M. A. Pouchon, C. Degueldre, and M. Dobeli, Prog. Nucl. Energy **38**, 275 (2001).
[16]C. Degueldre, M. Pouchon, M. Dobeli, K. Sickafus, K. Hojou, G. Ledergerber, and S. Abolhassani-Dadras, J. Nucl. Mater. **289**, 115 (2001).
[17]J. Jagielski, L. Thomé, C. Binet, F. Garrido, M. Mozetic, and A. Zalar, Nucl. Instrum. Methods Phys. Res. B **161–163**, 686 (2000).
[18]L. Thome, A. Gentils, F. Garrido, and J. Jagielski, Prog. Nucl. Energy **38**, 277 (2001).
[19]C. Hellwig, M. Streit, P. Blair, T. Tverberg, F. C. Klaassen, R. P. C. Schram, F. Vettraino, and T. Yamashita, J. Nucl. Mater. **352**, 291 (2006).
[20]M. Streit, W. Wiesenack, T. Tverberg, C. Hellwig, and B. C. Oberlander, J. Nucl. Mater. **352**, 349 (2006).
[21]T. M. Chen, S. M. Kauzlarich, and J. D. Corbett, J. Nucl. Mater. **151**, 225 (1988).
[22]E. H. P. Cordfunke and R. J. M. Konings, J. Nucl. Mater. **201**, 57 (1993).
[23]J. F. Ziegler, J. P. Biersack, and U. Littmark, *The Stopping and Range of Ion in Matter* (Pergamon, New York, 1985).
[24]N. Chauvin, S. Henry, H. Flocard, F. Fortuna, O. Kaitasov, P. Pariset, S. Pellegrino, M. O. Ruault, Y. Serruys, and P. Trocellier, Nuclear Instrum. Methods Phys. Res. B **261**, 34 (2007).
[25]M. O. Ruault, J. Chaumont, and H. Bernas, Nucl. Instrum. Methods Phys. Res. **209–210**, 351 (1983).
[26]L. Thomé, A. Gentils, F. Garrido, and J. Jagielski, Mater. Res. Soc. Symp. Proc. **792**, 49–60 (2004).
[27]L. Vincent and L. Thomé (unpublished).
[28]I. V. Afanasyev-Charkin and K. E. Sickafus, J. Nucl. Mater. **306**, 112 (2002).
[29]L. Thomé, A. Gentils, S. E. Enescu, H. Khodja, and T. Thomé, Nucl. Instrum. Methods Phys. Res. B **249**, 326 (2006).
[30]M. F. Ashby and L. M. Brown, Philos. Mag. **8**, 1649 (1963).
[31]J. Jagielski and L. Thomé, Vacuum **81**, 1352 (2007).
[32]J. F. Gibbons, Proc. IEEE **60**, 1062 (1972).
[33]N. Hecking, K. F. Heidemann, and E. Te Kaat, Nucl. Instrum. Methods Phys. Res. B **15**, 760 (1986).